OET | Opto-Electronic Technology

CN 51-1811/O4 ISSN (Print) 2097-6003 ISSN (Online) 2097-8006

Decoding subject-invariant emotional information from cardiac signals detected by photonic sensing system

Yukun Long, Rui Min*, Kun Xiao, Zhuo Wang, Lanfang Liu, Yifan Sun, Xiaoli Li, Zhaohui Li and Zeev Zalevsky

Citation: Long YK, Min R, Xiao K, Wang Z, Liu LF, Sun YF, Li XL, Li ZH, Zalevsky Z. Decoding subject-invariant emotional information from cardiac signals detected by photonic sensing system. *Opto-Electron Technol* **1**, 250010 (2025).

https://doi.org/10.29026/oet.2025.250010

Received: 9 November 2025; Accepted: 18 December 2025; Published online: 25 December 2025

OET | Opto-Electronic Technology
www.oejournal.org/oet

Article
December 2025, Vol. 1, No. 3

DOI: 10.29026/oet.2025.250010 | CSTR: 32419.14.oet.2025.250010

Decoding subject-invariant emotional information from cardiac signals detected by photonic sensing system

Yukun Long[1,2,3], Rui Min[3,4,5]*, Kun Xiao[6], Zhuo Wang[6], Lanfang Liu[3,4,5], Yifan Sun[7], Xiaoli Li[3,4,5], Zhaohui Li[8,9] and Zeev Zalevsky[10]

Abstract: Emotion recognition systems hold significant practical value due to the vital role emotions play in daily human life. Since cardiac activities are critically involved in the process of emotional arousal, developing emotion recognition systems based on cardiac signals is of great importance. However, inter-subject variability causes a major challenge for cross-subject emotion recognition and remains a key bottleneck for the practical application of emotion recognition systems. Here we report a photonic cross-subject emotion recognition system (PCERS) based on seismocardiography (SCG) signals, leveraging machine learning techniques driven by complex network feature engineering to decode subject-invariant emotional information from signals. In the cardiac activity monitoring component, we developed a photonic system for SCG signal detection and implemented a sample entropy-based signal processing pipeline. These designs enable precise cardiac activity monitoring as the foundation for emotion recognition. In the emotion recognition component, the complex network features extracted from SCG signals show significant differences between different emotional states, but no significant differences across subjects. Incorporating these features into the machine learning pipeline enables efficient cross-subject emotion recognition, achieving accuracies 81.25% in leave one-out (LOO) subject-independent emotion recognition. Results in this work suggested that PCERS has potential to contribute meaningfully to practical, real-life emotion recognition applications.

Keywords: photonic sensing; emotion recognition; machine learning; subject-invariant

Introduction

Emotion plays a vital role in daily human life[1], making emotion recognition valuable across a range of applications, such as mental health care[2], human-machine interaction[3–5], transportation safety[6], and educational support[7]. Emotion recognition methods are often based on various sources of information, including facial expressions[8,9], voice[10], self-assessments[11], and physiological signals[12]. Among these, physiological signals—reflecting neural activity associated with emotional states—are considered more objective and less susceptible to conscious control[13]. Changes in cardiac activity are critically involved in the process of emotional arousal, as cardiac sympathetic-vagal activity has been shown to play a leading and causal role in initiating emotional responses[14]. Furthermore, research has demonstrated the existence of cardiogenic control over affective behavioral states; for instance, optically evoked tachycardia in mice was found to markedly enhance anxiety-like behavior[15]. Moreover, the development of wearable devices has improved the convenience of cardiac activity monitoring in human daily life[16]. For these reasons, emotion recognition based on cardiac signals has attracted increasing attention in recent years. A range of emotion recognition systems have been developed utilizing signals that reflect cardiac

Received: 9 November 2025
Accepted: 18 December 2025

[1]Department of Systems Science, Faculty of Arts and Sciences, Beijing Normal University, Zhuhai 519087, China; [2]School of Systems Science, Beijing Normal University, Beijing 100875, China; [3]Department of Psychology, Faculty of Arts and Sciences, Beijing Normal University, Zhuhai 519087, China; [4]Faculty of Psychology, Beijing Normal University, Beijing 100875, China; [5]Center for Cognition and Neuroergonomics, State Key Laboratory of Cognitive Neuroscience and Learning, Beijing Normal University, Zhuhai 519087, China; [6]Department of Physics, Faculty of Arts and Sciences, Beijing Normal University, Zhuhai 519087, China; [7]Service OPERA-Photonique, Université libre de Bruxelles, B-1050 Brussels, Belgium; [8]Guangdong Provincial Key Laboratory of Optoelectronic Information Processing Chips and Systems and School of Electronics and Information Technology, Sun Yat-sen University, Guangzhou 510006, China; [9]Southern Laboratory of Ocean Science and Engineering, Zhuhai 519000, China; [10]Faculty of Engineering and Nano Technology Center, Bar-Ilan University, Ramat Gan 5290002, Israel.
*Correspondence: R Min, E-mail: ruimin@bnu.edu.cn

activity, such as electrocardiography (ECG)[17−20], photoplethysmogram (PPG)[21−23], and mechanical cardiac vibration signals, commonly known as seismocardiography (SCG)[24−26]. These systems employ machine learning or deep learning techniques to identify different emotional states from the physiological patterns embedded in these signals.

Building on existing research in emotion recognition, it is evident that systems based on cardiac signals generally consist of two key components: a cardiac signal extraction component and a classification component employing machine learning techniques to identify emotional states from features derived from cardiac signals[27]. Among these two components, a robust and efficient cardiac signal extracting method is the base of precise emotion recognition[24]. In recent years, cardiac activity monitoring using optical fiber sensors has attracted increasing attention, owing to the unique advantages of these sensors in enabling robust and efficient signal extraction. These advantages include high sensitivity, electrical safety, flexibility, rapid response time, biocompatibility, immunity to electromagnetic interference, and resistance to electrochemical corrosion[28−30]. However, despite the high performance of various optical fiber sensors in cardiac activity monitoring[31−36], these technologies face a universal challenge shared with other physiological sensing methods: motion artifacts induced by body movements and physiological activities[37]. Motion artifacts can affect cardiac activity monitoring and subsequently impact emotion recognition. To overcome this issue, a sample entropy-based signal processing pipeline is employed in this work. Given that cardiac activity signals are quasi-periodic time series data[38], sample entropy analysis effectively identifies signal components with low complexity that align with this quasi-periodic nature, thereby ensuring accurate cardiac monitoring under the influence of motion artifacts.

In the classification component of cardiac activity based emotion recognition systems, time-domain heart rate variability (HRV), frequency-domain HRV, and nonlinear features (such as entropy-based measures and Poincaré plot analysis) are commonly extracted as inputs to machine learning models[27]. However, these approaches often face limitations in subject-independent emotion recognition due to inter-subject variability. Specifically, performance tends to degrade when the training and testing data are drawn from different subjects[39]. This challenge is not unique to cardiac-based methods, similar issues arise in emotion recognition using other physiological signals, such as electroencephalography (EEG). The need for extensive subject-specific training data makes training procedure laborious and time-consuming, representing a major bottleneck in practical applications[40]. Cardiac activity monitoring has become increasingly practical for daily life applications, largely due to the rapid development of wearable devices[41]. However, facing the main bottleneck of practical application: subject independent emotion recognition, current methods of cardiac activity based emotion recognition systems remain more limited than those developed for systems based on other physiological signals[40,42,43]. Changes, rather than absolute values, of physiological features extracted from cardiac activity signals have been leveraged to mitigate inter-subject variability[24]. However, an accuracy gap of 14.7% still remains between subject-independent and subject-dependent emotion recognition.

Efficient cross-subject emotion recognition is of great importance for both the theoretical advancement and practical application of emotion recognition systems[40,44]. To address current limitations caused by inter-subject variability, we present a photonic cross-subject emotion recognition system (PCERS) that achieves high accuracy in subject-independent emotion recognition. The cardiac activity monitoring component serves as the foundation for emotion recognition in PCERS. In this component, a photonic sensing system equipped with a photonic vibration sensing device (PVSD) is employed to detect cardiac signals due to its aforementioned advantages. Additionally, the aforementioned sample entropy-based signal processing pipeline ensures efficient and robust cardiac monitoring under both artifact-free and motion artifact conditions, achieving heart rate monitoring accuracies of 99.64% and 98.32%, respectively. To decode subject-invariant emotional information from signals, we introduce a complex network approach that constructs networks from cardiac signals and extracts topological features from them. An effective strategy to mitigate inter-subject variability for cross-subject emotion recognition is to extract subject-invariant features that vary significantly across emotional states but remain consistent across individuals[39]. Experimental results in this work demonstrate that the SCG-derived network features exhibit significant differences among emotional states while showing no significant variation across subjects. Incorporating these features ensures strong performance in cross-subject emotion recognition, achieving an accuracy of 81.25% in recognizing four emotions—fear, joy, sadness, and relaxation—under leave-one-out (LOO) cross-validation. This result surpasses previous studies, which reported accuracies of 72.3%[24] and 72.1%[45]. Furthermore, the accuracy gap between subject-dependent and subject-independent emotion recognition in our study is only 1.04% and 2.75% in two respective comparison settings, significantly lower than the 14.7% gap reported in previous study[24], demonstrating the consistency of our system across both subject-dependent and subject-independent scenarios.

Results

Photonic cross-subject emotion recognition system (PCERS)

Figure 1 demonstrates an overview of PCERS, emphasizing its core principle, fundamental components, and capability in mitigating accuracy gap between subject-dependent and subject-independent emotion recognition. Figure 1(a) illustrates the core principle of PCERS. According to the James-Lange theory, physiological changes, which are initiated by environmental stimuli, are subsequently interpreted by the central nervous system, generating emotions and feelings[14]. This theoretical framework suggests that emotions can be monitored by measuring physiological changes, such as cardiac activity, which serve as a key biomarker of autonomic arousal[46].

To precisely monitor cardiac activity, a photonic sensing system equipped with a PVSD was designed, which is demonstrated in Fig. 1(b). The basic working mechanism of PVSD relies on detecting displacement variations in output speckle patterns to measure cardiac-induced mechanical

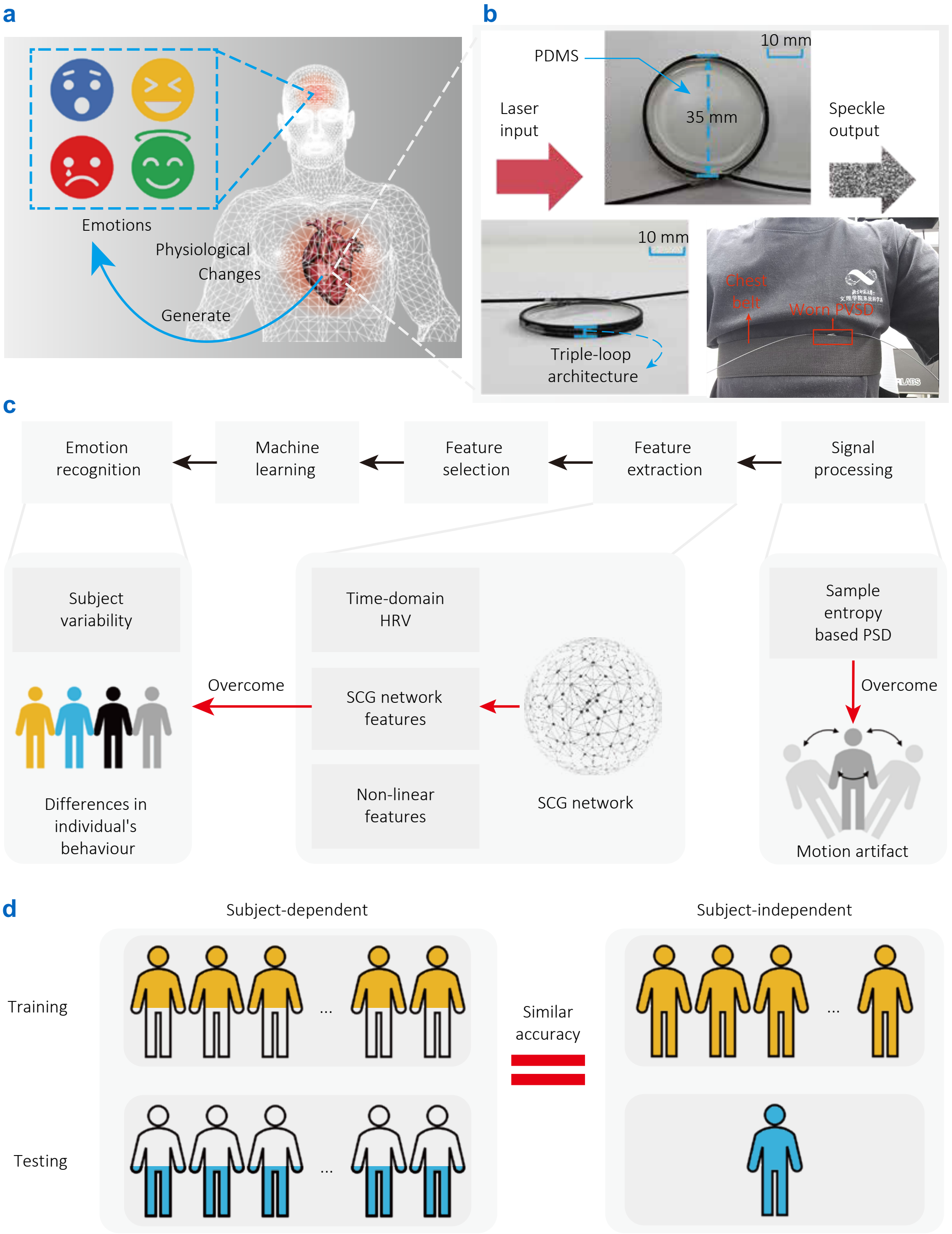

Fig. 1 | An overview of PCERS. (**a**) Core priciple of PCERS. Physiological changes are subsequently interpreted by the central nervous system, generating emotions and feelings. (**b**) An overview of the PVSD. (**c**) The signal processing and classification pipeline of PCERS. (**d**) The key advantage of PCERS lies in its capability to mitigate subject variability, which is reflected on the similar accuracy between subject-dependent and subject-independent cross-validation methods.

vibrations at the chest surface, which is commonly known as SCG[47]. The speckle patterns are created when coherent light propagates through polymer optical fiber (POF) utilized in PVSD. To enhance the sensitivity of PVSD, the POF is configured into a triple-loop architecture, with a diameter of 35 mm[48]. Additionally, to improve PVSD's robustness, polydimethylsiloxane (PDMS) is employed to secure and encapsulate the triple-loop architecture. The preparation method of PVSD is illustrated in the Methods section. Sensor placement affects the accuracy of cardiac activity monitoring. Since the mitral valve auscultation area provides reliable measurements[49], the PVSD is positioned at this location and secured with a chest belt to ensure accurate data acquisition, as shown in Fig. 1(b).

Figure 1(c) illustrates the signal processing and classification pipeline of PCERS. Upon acquisition of raw SCG signals, they undergo a processing stages to obtain clean signals. This cascade utilizing a sample entropy-based power spectral density (PSD) analysis to mitigate in-band motion artifacts. Features including time-domain HRV features, nonlinear features and SCG network features are extracted from signals. Specifically, the SCG network features are extracted from network (structure of SCG network is demostrated in Supplementary information of Fig. S1) build from SCG signals, utilized to mitigate subject variability. Distinct features undergo a feature selection process during training process of machine learning.

Figure 1(d) demonstrates the cross-subject emotion recognition capability of PCERS. This adavantage reflects on the similar accuracy between subject-dependent and subject-independent cross-valiation methods. In subject-dependent and subject-independent methods, the training and testing data are derived from the same subjects or different subjects, respectively. The accuracy gap between the average cross-validation results of subject-independent and subject-dependent methods is less than 3% in our experiment, confirming PCERS's ability to mitigate subjects variability.

Working mechanism and characterization of the cardiac activity monitoring component

The photonic sensing system and signal processing pipeline constitutes the cardiac activity monitoring component of PCERS. Figure 2 illustrates the working mechanism and characterization of this component. The working mechanism of photonic sensing system is demonstrated in Fig. 2(a). When coherent light (laser) propagates through PVSD, the equally excited multiple modes it generates interfere and create a speckle pattern[48]. The far-field speckle pattern image can be captured by a defocused camera. The specific models of the supporting devices used in the photonic sensing system, including the industrial camera and laser, are detailed in the Methods section. In this work, the region of interest (ROI) is confined to the speckle area, with the grayscale values of pixels outside this ROI set to zero. A speckle image preprocessing algorithm is used to achieve this, as specifically detailed in the Methods section. When a heartbeat occurs, body vibrations cause deformation in PVSD, leading to perturbations in the propagation medium of the multiple modes. As a result, pixel-wise intensity changes occur between adjacent frames of the speckle pattern images. Therefore, body vibrations caused by cardiac activity can be captured by detecting sum of the pixel-wise intensity changes in the far-field speckle pattern images[48]. To evaluate PVSD's performance, an elastic ball was dropped freely from a height of 5 cm onto it and promptly rebounded, generating a transient pulse in the sensor's output. This experimental setup was (commonly) used to measure sensor's response and recovery time[50]. The results of this experiment, presented in Fig. 2(b), indicate an average response time of 15.09 ms and an average recovery time of 11.32 ms across three trials, which demonstrates the same performance with the existing works[36,50].

Figure 2(c) illustrates the signal processing pipeline of PCERS. Hamming windows are first applied to the raw signal, followed by the utilization of a band-pass Butterworth filter on each windowed signal. This filter reduces noise outside the normal heart rate range, which is set to a bandwidth of 0.6 Hz to 3.0 Hz[51]. The most critical aspect of clean SCG signal extraction is the accurate selection of the heart rate frequency component, which allows for the precise extraction of the SCG signal. To achieve this, the fast Fourier transform (FFT) is employed to the windowed and filtered signal. However, while the bandpass filter effectively reduces noise outside the normal heart rate range, motion artifacts may still introduce in-band noise, which is a common issue in the field of biosignal sensing[52]. To address this issue, we combine frequency domain magnitude analysis with the sample entropy method. The top four highest magnitude frequency components are selected, and the inverse fast Fourier transform (IFFT) is applied to convert them into time domain signals. The sample entropy of these signals is then calculated (the calculating method of sample entropy is illustrated in the Methods section). Sample entropy is commonly used to measure the complexity of biosignals[53]. As a type of pseudoperiodic signal, SCG signals typically exhibit low complexity, which is reflected in their low sample entropy values. Sample entropy based selection is applied among these top four highest magnitude frequency components. The algorithm prioritizes selecting the components whose corresponding time-domain signal exhibits the lowest sample entropy within the resting heart rate range. The selected component is considered the heart rate frequency component, and its corresponding time-domain signal is regarded as the SCG signal.

The effectiveness of this method for extracting a clean SCG signal from raw signals with in-band noise caused by motion artifacts is confirmed through our experiments. The experimental setup is detailed in the Methods section, and

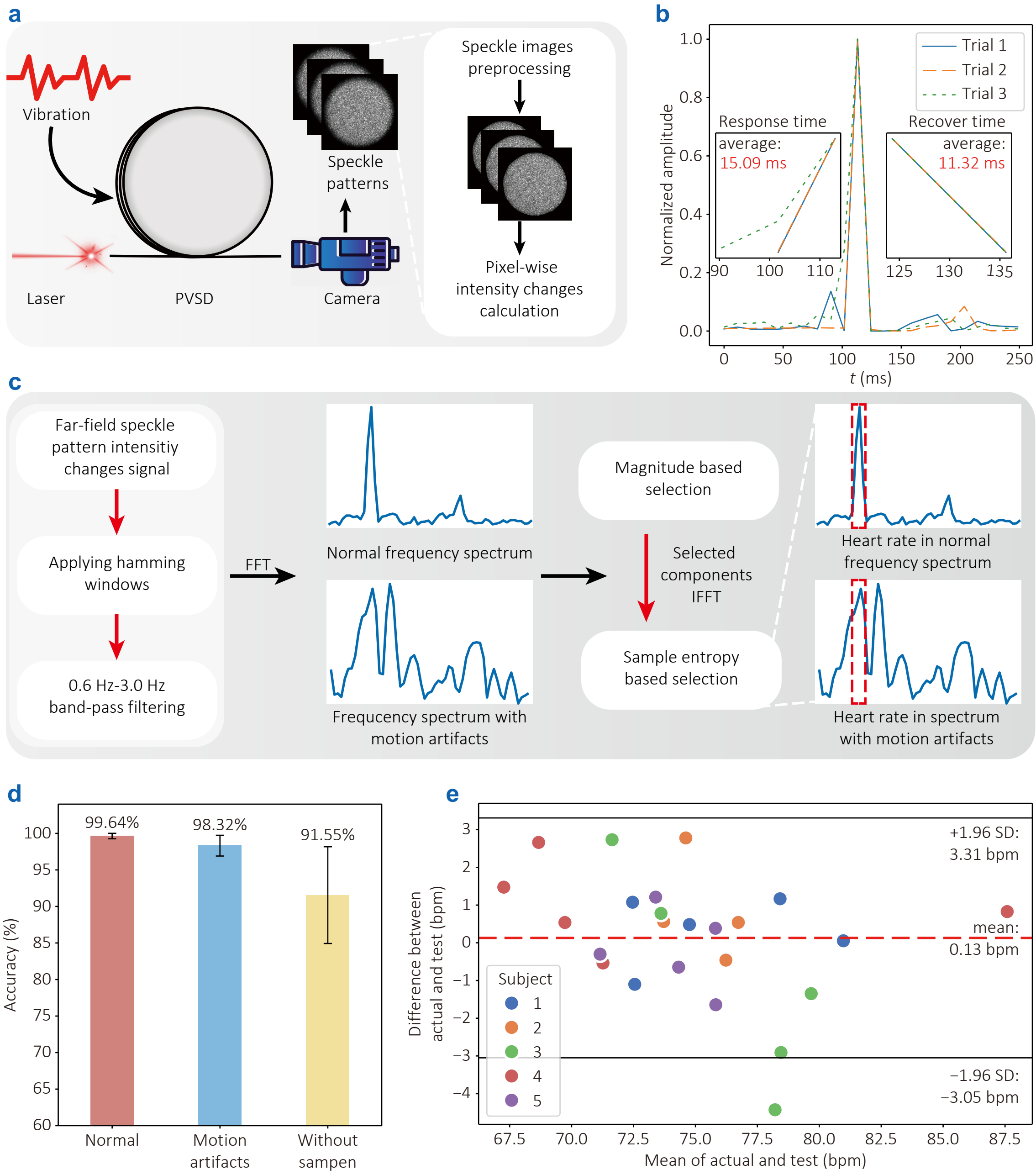

Fig. 2 | Working mechanism and characterization of the SCG signal extracting component. (**a**) The working mechanism of PVSD. (**b**) The experimental result of the response and recovery time of PVSD, indicate an average response time of 15.09 ms and an average recovery time of 11.32 ms. (**c**) The signal processing pipeline of PCERS, highlighting the sample entropy-based frequency component selection, which aims to mitigate in-band noise caused by motion artifacts. (**d**) Experimental validation of SCG signal extraction under motion artifacts. The error bars represent one standard deviation of accuracy. The control group (artifact-free) achieved 99.64% accuracy, while the experimental group (with motion artifacts) achieved 98.32%. In comparison, the method without sample entropy reached only 91.55%, demonstrating the effectiveness of incorporating sample entropy. (**e**) Bland-Altman plot illustrating the heart rate monitoring error with motion artifacts utilizing the sample entropy method, illustrating a mean error of 0.13 bpm. Nearly all data points fall within the range of the mean ± 1.96 standard deviations.

the result of this experiment is illustrated in Fig. 2(d). The control group, conducting heart rate monitoring under motion artifact-free conditions, exhibited a mean accuracy of 99.64%. The experimental group, which involved heart rate monitoring with motion artifacts, yielded a mean accuracy of 98.32%. As a comparison, the method without applying sample entropy achieved a mean accuracy of only 91.55% in the presence of motion artifacts, thereby validating the effectiveness of incorporating sample entropy in our approach. Meanwhile, the cardiac monitoring method using sample entropy shows significantly greater consistency compared to the baseline, as demonstrated by the error bars in Fig. 2(d). Figure 2(e) presents the Bland-Altman plot for the results of heart rate monitoring with motion artifacts, showing a mean error of 0.13 bpm (beat per minute). Nearly all data points fall within the range of the mean ±1.96 standard deviations, corresponding to an interval of [−3.05, 3.31] bpm.

The characterization of the SCG signal extraction component was also evaluated from several other aspects, including testing the performance of different designs PVSD's structure, assessing the durability of PVSD, and evaluating the its robustness against ambient light. These characterization and experiments are detailed in the Methods section of this article.

Experimental setup and feature engineering for emotion recognition

Figure 3 illustrates the experimental setup and feature engineering for emotion recognition. PCERS classifies human emotions into four quadrants of the established valence-arousal model: high arousal and high valence (HAHV), high arousal and low valence (HALV), low arousal and high valence (LAHV), and low arousal and low valence (LALV). PCERS's emotion recognition performance has been validated by recognizing the four basic emotions—joy, fear, sadness, and relaxation—which are located in the four quadrants respectively. The experimental setup of emotion recognition is demonstrated in Fig. 3(a). In this experiment, the subjects were asked to watch emotion-eliciting video clips designed to evoke joy, fear, relaxation and sadness. Each emotion was associated with 6 video clips, and the experiment was conducted with eight subjects, resulting in a total of 192 trials of this experiment. In every single trial, a 2 min video clip was displayed. The first minute was intended to elicit the subject's emotional response, followed by the second minute during which the SCG signals were recorded. After the cardiac activity monitoring phase, the subject performed a self-assessment of valence and arousal levels. A trial was considered valid when the subject's self-reported valence and arousal states were consistent with the target emotion of the video clip. In such cases, the emotion associated with the video stimulus was treated as the ground truth label for that trial. At the end of each trial, the participant took a 2 min break to restore to neutral state. Each subject participated in the experiment between 3:00 p.m.–4:00 p.m., and completed only one trial per emotion to avoid fatigue.

As aforementioned, we have introduced a novel application of complex network methods in the field of biosignal emotion recognition to overcome the accuracy gap between subject-dependent and subject-independent methods, which is primarily attributed to the physiological differences among distinct individuals. The construction method of SCG network is illustrated in Fig. 3(b). This method is inspired by the research utilizing complex network method to analyse ECG signal[54]. In this procedure, the processed SCG signal is first split into a series of *RR* intervals as demonstrated in Fig. 3(c). Subsequently, to obtain the adjacency matrix, the distance between each pair of *RR* intervals[55] is calculated, as below:

$$\boldsymbol{D}_{ij}=\min_{l=0,1,\cdots,\left|l_j-l_i\right|}\frac{1}{\min\left(l_i,l_j\right)}\sum_{k=1}^{\min\left(l_i,l_j\right)}\left\|X_k-Y_{k+l}\right\| . \tag{1}$$

To calculate the distance between *RR* intervals i and *RR* intervals j with different length (l_i, l_j), a rectangular window of the same length as the shorter *RR* interval is employed. This window traverses the entire longer interval by moving one time step at a time. At each step, the Euclidean distance between the shorter interval and the windowed segment of the longer interval is calculated (X_k in Eq. (1) represents data point in shorter interval and Y_{k+l} represents data point in longer interval).

The minimum value from this series of calculated distances is taken as the distance between the two intervals, resulting in an adjacency matrix $\boldsymbol{D}$ where each element represents the calculated distance. To align with the principle of shifting from absolute measures of physiological states to relative values, adjacency matrix is further binarized. The threshold-edge count function, which counts the number of edges in the network based on different threshold values, is used to determine the appropriate binary threshold[55]. The threshold value corresponding to the inflection point of this function is selected (as illustrated in Fig. 3(d)): distances greater than this threshold are set to zero, while those below it are retained. This approach allows for the creation of a binary adjacency matrix. It is sufficient that the distances between every two *RR* intervals are automatically encoded in the SCG network. As demonstrated in Fig. 3(e), there is a linear relationship between the shortest path in the SCG network and the distances between *RR* intervals, which yields an R^2 score of 1.000.

We have noticed that assortativity is existed in the SCG networks. As shown in the joint degree distribution figure (Fig. 3(f)), the nodes of SCG netowrk are prefer to attach with the nodes which have the similar degree. The attachment modes of nodes in the SCG network reflect the similarity between *RR* intervals, encapsulating valuable physiological information. Therefore, the topological features of the SCG network are extracted and utilized as input for our machine learning model.

In addition to SCG network features, traditional time-domain HRV features and non-linear features are also extracted. To demonstrate importance of these features, permutation importance was calculated across two dimensions: arousal and valence (all features and permutation importance calculation method are detailed in the Methods section). As demonstrated in Fig. 3(g), in the arousal dimension, all four most important features were derived from the SCG network. Figure 3(h) illustrated the features' importance in valence dimension. The top four most important features were time-domain frequency features (PNN20, SDNN), one Poincaré plot feature (SD2), and one

Fig. 3 | The experimental setup and feature engineering for emotion recognition. (**a**) Experimental setup for emotion recognition. (**b**) Construction method of the SCG network. Here, D denotes the adjacency matrix, l_i and l_j represent lengths of two intervals, X_k and Y_{k+l} refer to data points in the shorter and longer intervals, respectively. (**c**) *RR* intervals of the raw and processed SCG signal. (**d**) The method for selecting the binary threshold value. (**e**) Linear relationship between the shortest path in the SCG-binary network and the distances between *RR* intervals. (**f**) Joint degree distribution of the SCG network. Permutation importances of features in (**g**) arousal dimension and (**h**) valence dimension.

SCG-binary network topological feature. To enhance the emotion recognition performance of PCERS, these features underwent permutation importance-based selection processes during training process of machine learning, as detailed in Methods section.

Results of emotion recognition

Figure 4 demonstrates the results of emotion recognition experiments. The machine learning model used in this experiment is a support vector machine (SVM) with radial basis function (RBF) kernel, as detailed in the Methods section. To evaluate the performance of the PCERS in both subject-dependent and subject-independent scenarios, different kinds of cross-validation methods were employed. In the subject-dependent scenario, 8-fold and 4-fold cross-validation were applied, where 1/8 and 1/4 of the data, respectively, were reserved for test dataset in each iteration. For the subject-independent scenario, the LOO and leave-two-subjects-out (LTO) cross-validation methods were employed. In each iteration, the data from one or two subjects were excluded in test dataset, respectively. Both methods exhaustively traversed all possible combinations of selecting one or two subjects from the total of eight subjects to ensure comprehensive evaluation. As dtailed in Methods section, in each iteration of cross-validation, a data scaler is fitted on the training dataset and then used to scale both the training and test datasets separately. Next, feature extraction is performed on the training dataset, followed by feature selection to obtain a subset of informative features for model training. The selection frequency of each feature is demonstrated in Supplementary information of Fig. S2. The trained model is then evaluated using the corresponding selected features from the test dataset.

The average confusion matrix, macro-averaged receiver operating characteristic (ROC) curve, and average F1 score for the 8-fold, LOO, 4-fold, and LTO cross-validation methods are presented in Fig. 4(a–d), respectively (the ROC curve and precision of each emotion for these four cross-validation methods are demonstrated in the Supplementary information of Fig. S3 and Fig. S4, respectively). The test sets in the 8-fold and LOO cross-validation methods, as well as in the 4-fold and LTO methods, were of same scale. Therefore, performance comparisons were conducted within these two groups. The mean accuracy for these four cross-validation methods was 82.29%, 81.25%, 80.73%, and 77.98%, respectively. These results are higher than those reported in existing studies on subject-independent emotion recognition[24,43]. The accuracy difference between the 8-fold and LOO cross-validation was 1.04%, while the difference between the 4-fold and LTO cross-validation was 2.75%. Comparing the macro average ROC curves, the area under curve (AUC) of these four cross-validation methods are 0.93, 0.93, 0.93, and 0.92, respectively. Regarding the F1 scores, the maximum F1 score difference for the same emotion was 0.07 in both comparative groups: between 8-fold and LOO methods, and between 4-fold and LTO approaches. To provide a more detailed demonstration of the emotion recognition performance for each participant, the average accuracy of each subject under each cross-validation method is presented in Fig. 4(e). Furthermore, we replaced the classifier with other machine learning models (KNN, linear SVM, and XGBoost) and found that the accuracy gap between subject-independent and subject-dependent emotion recognition remained low, as demonstrated in the Supplementary information of Figs. S5–S7. These results not only confirm the emotion recognition performance of the PCERS but also demonstrate its ability to mitigate subject variability.

Statistical analysis for the extracted features

To analyze the differences in extracted features across different emotions and subjects and to further enhance the interpretability of our method, we conducted a statistical analysis. Methods of statistical analysis are detailed described in the Methods section. The results of the statistical analysis are presented in Fig. 5.

Firstly, the differences in extracted features across different emotions were analyzed. The test results for SCG network features and time-domain HRV are presented in Fig. 5(a–h), while the results for nonlinear features are provided in the Supplementary information of Fig. S8(a–g). The p-values reflecting feature differences across emotions for all features are presented in Supplementary information of Fig. S8(h). The title of each boxplot indicates the feature's name and the significance level of differences across the four emotions, represented by significance stars. Pairwise test results are depicted within each boxplot using significance bars, with significance stars and effect sizes displayed above them.

Figure 5(a–d) demonstrates the statistical tests results of the four SCG network features. By examining the effect sizes, we observed that the numerical values of the features tend to be higher when subjects are in a lower arousal state, such as during relaxation and sadness. The attachment patterns of nodes in the SCG network reflect the similarity between heartbeats. Higher numerical values of SCG network features suggest that heartbeats exhibit greater similarity when the emotional state is characterized by lower arousal levels. Figure 5(e–h) demonstrates the statistical tests results of time-domain HRV. The effect sizes indicate that the numerical values of the features tend to be higher when the emotional state is characterized by higher valence levels. This suggests greater variability in heartrate when subjects experience a higher valence state. Based on these observations, we found that the feature space constructed by the most important features in the arousal and valence dimensions (GCC and PNN20) can

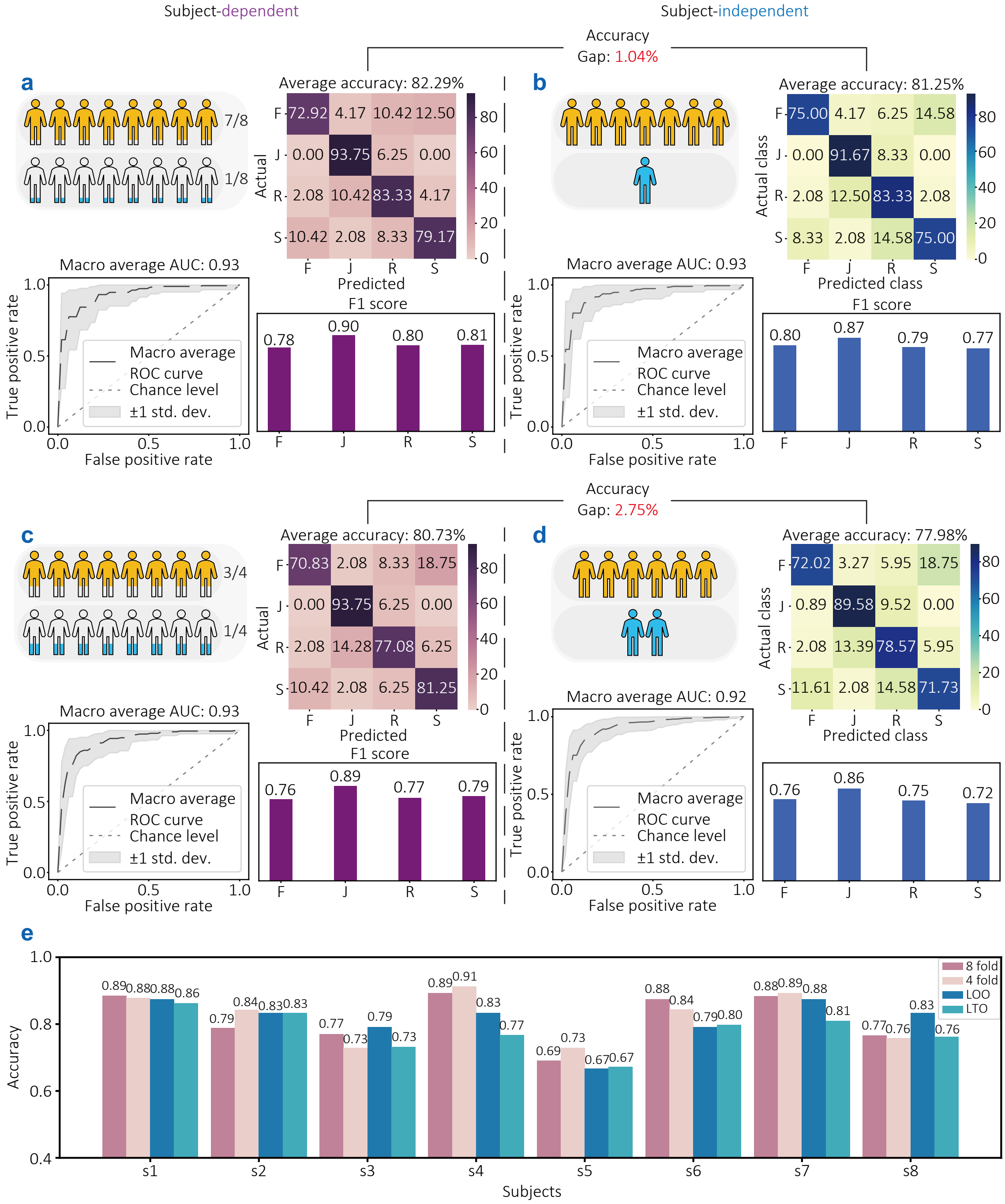

Fig. 4 | The results of emotion recognition experiments. The training-testing set splitting method, confusion matrix, macro-averaged ROC curve, and average F1 score for (**a**) the 8-fold, (**b**) LOO, (**c**) 4-fold, and (**d**) LTO cross-validation methods. The accuracy difference between the 8-fold and LOO cross-validation was 1.04%, while the difference between the 4-fold and LTO cross-validation was 2.75%. AUC of these four cross-validation methods are 0.93, 0.93, 0.93, and 0.92, respectively. The maximum F1 score difference for the same emotion were 0.07 in both comparative groups. (**e**) The average accuracy of each subject under each cross-validation method.

approximately divided into the four quadrants of the valence-arousal model, as shown in Fig. 5(i). The kernel density estimation (KDE) plot shown in Fig. 5(j) further illustrates the distribution of these two features.

The results of the analysis of feature differences across subjects are presented in Fig. 5(k). It is evident that SCG network features did not show significant differences across subjects, as indicated by high *p*-values. In contrast, some traditional time-domain HRV and nonlinear features exhibited significant differences across subjects, as demonstrated by the significance stars in the figure. This confirms the effectiveness of utilizing the SCG network in overcoming physiological differences among individuals and decoding subject-invariant emotional information.

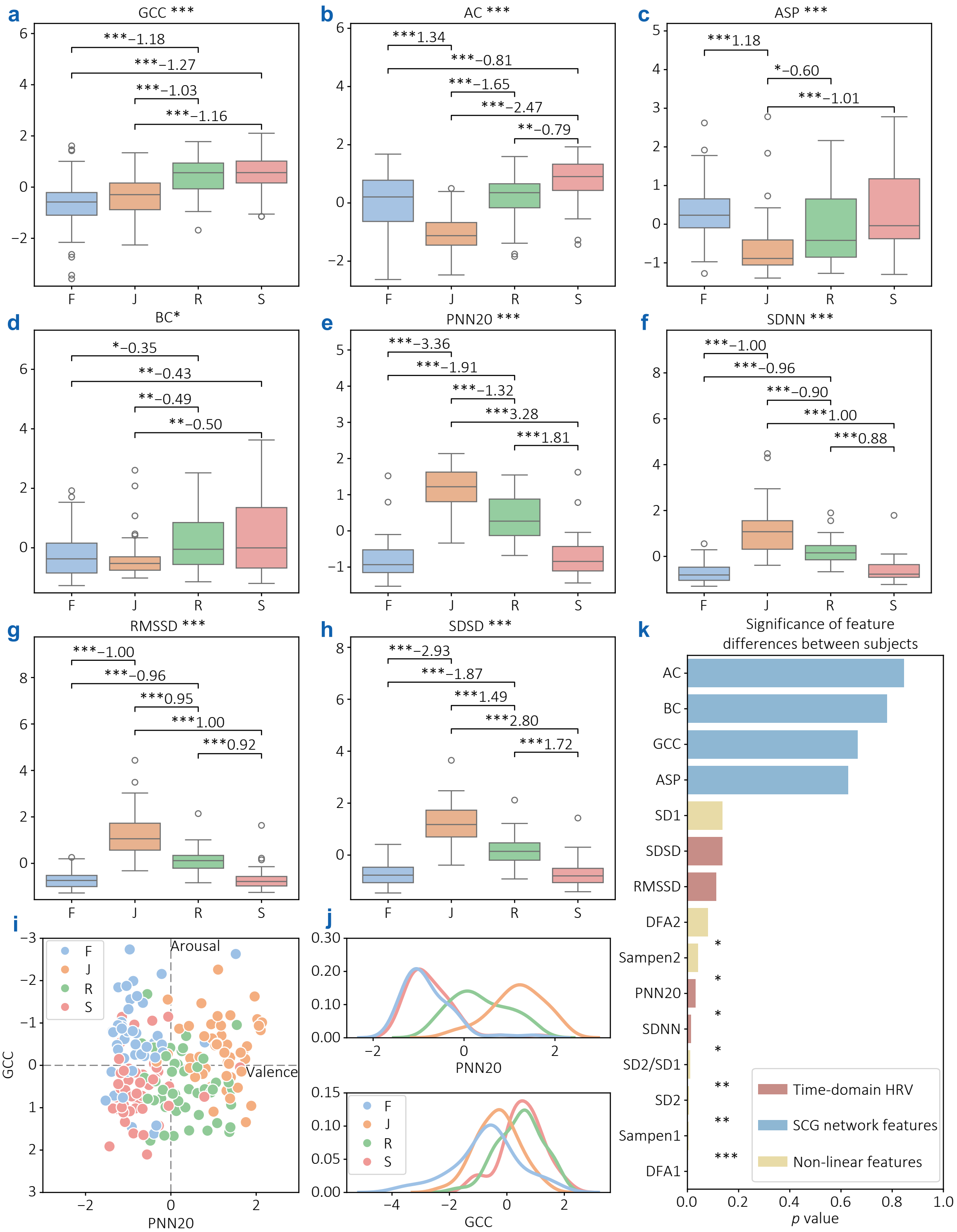

Fig. 5 | The results of the statistical analysis. (**a-d**) Differences in SCG network features across emotions. Each boxplot title shows the feature name and significance level ($p<0.05$: *, $p<0.01$: **, $p<0.001$: ***). Pairwise test results are indicated within the boxplots, with significance bars, along with significance stars and effect sizes displayed above them. (**e-h**) Differences in time-domain HRV across emotions. (**i**) Feature space constructed by the most important features in the arousal and valence dimensions can be approximately divided into the four quadrants of the valence-arousal model. (**j**) KDE plot for the PNN20 and GCC. (**k**) The results of the analysis of feature differences across subjects, illustated by *p* value and significance stars.

Methods

Preparation of PVSD

The preparation process of PVSD including following steps, as illustrated in the flowchart in Supplementary information of Fig. S9(c). First, the silicone elastomer base and curing agent are weighed in a mass ratio of 10：1 to prepare the PDMS solution (4.0 g of base and 0.4 g of curing agent). The PDMS material is chosen because of its cost-effective platform and strain sensor capability[56]. Next, the silicone elastomer base and curing agent are thoroughly mixed. Subsequently, the mixture is allowed to stand for 10 minutes to facilitate defoaming. Three POF loops are then arranged within a 3D-printed mold, which is filled with the well-mixed PDMS solution to encapsulate the loops. Finally, the assembly is left to cure for 24 h before demolding to obtain the POF sensor.

Additionally, experiment was conducted to evaluate the effectiveness of PDMS encapsulation and the performance of sensors equipped with fibers of different core diameters. This experiment evaluated the accuracy and signal-to-noise ratio (SNR) of various PVSD designs, including a structure without PDMS encapsulation and PVSD equipped with fibers having core diameters of 250 μm, 500 μm, and 750 μm in the heart rate monitoring function. The results are illustrated in Supplementary information of Fig. S10(b, c). It is evident that the use of PDMS encapsulation significantly increases both the accuracy of heart rate monitoring and the SNR of the SCG signal. Among the fibers of varying core diameters, PVSD equipped with a core diameter of 500 μm exhibited the highest mean accuracy and mean SNR, at 99.64% and 14.92 dB, respectively. Therefore, the POF with a core diameter of 500 μm was selected for the preparation of PVSD.

Devices utilized in the SCG signal extracting component

Apart from PVSD, other devices were utilized in the SCG signal extraction component. A benchtop laser (THORLABS, S1FC660, 650 nm) served as the coherent light source to generate the speckle pattern in the POF sensor. An industrial camera (HIKROBOT, MV-CU013-A0UC) equipped with a 12 mm focal length lens (HIKROBOT, MVL-HF1228M-6MPE) was used to capture the far-field speckle pattern images. The laser power was set to 2 mW, while the exposure time and frame rate were set to 500 μm and 88 Hz, respectively.

Temerature consistency of PVSD

To verify the stability of the PVSD under different temperature conditions, we designed the following experiment. The PVSD was placed on a temperature-controlled heating stage, with a 660 nm laser serving as the light source and a Thorlabs optical power meter used as the detector. The output optical power was measured at temperatures of 30, 40, 50, 60, and 70 °C, as shown in Supplementary information of Fig. S11. Across this temperature range, the optical power varied from −12.41 dBm to −12.30 dBm. Notably, within the typical temperature range encountered during contact with the human body (30–40 °C), the optical power fluctuation was only 0.02 dBm, demonstrating the stability of the sensor in response to temperature variations.

Speckle images preprocessing algorithm

To accurately extract raw SCG signals from far-field speckle images, a speckle image preprocessing algorithm is employed, as detailed in the Supplementary information of Fig. S12. These raw speckle images contain three RGB channels. To enhance signal extraction accuracy, they are first converted to grayscale. Next, the region of interest (ROI) is restricted to the speckle area, with the grayscale values of pixels outside this ROI set to zero. The first frame of the grayscale speckle images serves as the basis for creating a binary mask. To ensure smooth edges in the mask while retaining sufficient information from the grayscale images, Gaussian filtering is applied to the selected frame. After that, the OTSU algorithm is employed to automatically detect the edges of the speckle pattern, allowing for automatic selection of the ROI in the grayscale speckle images. The selected image is then binarized, with grayscale values of pixels within the ROI set to one and those outside set to zero, resulting in the creation of a binary mask. This binary mask is used for pixel-wise multiplication with each original grayscale speckle image, yielding processed speckle images that retain the original grayscale values within the ROI, while the grayscale values outside the ROI are set to zero.

Calculating method of the pixel-wise intensity changes

As a type of multimode optical fiber (MMF), POF operates on the same principle as common MMF sensors to detect vibration. When coherent light propagates through a POF, the equally excited multiple modes it generates interfere and create a speckle pattern[48]. The far-field light speckle distribution of the fiber results from the superposition of all mode amplitudes. For a pixel (x,y), the complex amplitude $A(x,y)$ gives rise to the measurable intensity pattern captured by the camera as

$$I(x,y) = |A(x,y)|^2 \ . \tag{2}$$

When a heartbeat occurs, body vibrations cause deformation in the POF, leading to perturbations in the propagation medium of the multiple modes. These perturbations cause deviations in both amplitude and phase, depending on the mode index, consequently altering the far-field speckle pattern. As a result, there will be pixel-wise intensity changes between adjacent frames of the speckle pattern images. To detect subtle mechanical perturbations (e.g., from heartbeats), we analyze temporal changes in speckle intensity by computing the difference between consecutive frames:

$$\Delta I_f^2 = \sum_{\text{All pixels}} |I_{f+1}(x,y) - I_f(x,y)|^2 \ , \tag{3}$$

where f represents the frame number and (x,y) represents the pixels in the far-field speckle pattern images. Equation 3 is employed to calculate the square sum of pixel-wise intensity changes in the far-field speckle pattern videos recorded by the defocused camera, frame by frame. This calculation procedures the raw SCG signal.

Sample entropy

In this work, sample entropy analysis is employed to mitigate the in-band noise introduced by motion artifacts. The calculation of sample entropy involves the following steps: First, the time-domain signals, obtained by applying the IFFT to the selected frequency components, are segmented into splits of length l. Then, the Chebyshev distance is computed between every pair of these splits as follows:

$$d_{PQ}^l = D_{\text{Chebyshev}}(P^l, Q^l) = \max_i(|p_i - q_i|) \ , \tag{4}$$

where P^l and Q^l denote different signal splits, and p_i and q_i represent their respective standard coordinates. For a given signal split P^l, the number of splits with a Chebyshev distance less than a predefined threshold r is counted and denoted as $\Psi_P^{l,r}$. The ratio of $\Psi_P^{l,r}$ to the total number of signal splits is then computed as $\Psi_P^{l,r}$. The average of this ratio across all splits is represented by $\Phi^{l,r}$. Next, the segment length is increased to $l+1$, and $\Phi^{l+1,r}$ is computed accordingly. Finally, the sample entropy is determined using the following equation:

$$\text{Sampen}(l,r) = -\ln\left[\frac{\Phi^{l+1,r}}{\Phi^{l,r}}\right] \ . \tag{5}$$

In this work, we set $l = 1$ and $r = 0.2$ std(signal), where std(signal) denotes the standard deviration of the signal.

R-peak detection algorithm

To detect cardiac peaks from the processed physiological signals, a multi-stage adaptive thresholding algorithm was implemented. The algorithm consists of three primary steps: moving-average baseline estimation, dynamic threshold generation, and valid peak identification. Firstly, two moving averages with different window lengths are computed from the input signal, where the short-time average captures beat and the long-time average represents the rhythm. A dynamic threshold is then generated by adding an adaptive offset—proportional to the mean signal amplitude—to the long-time average, allowing the threshold to automatically adjust to signal intensity and baseline changes. Segments exceeding this threshold are identified as potential heartbeat intervals, within which the local maxima are extracted as candidate peaks. To avoid false detections, a minimum peak width threshold is applied to remove noise-induced peaks. Finally, the detected peaks and their corresponding amplitudes are retained as valid cardiac events.

Experiment validation SCG signal extraction under motion artifacts

We designed an experiment to validate SCG signal extraction under motion artifacts and confirm the effectiveness of our method in mitigating the resulting in-band noise. In this experiment, subjects were instructed to perform three types of movements: moving the body forward and backward, moving it left and right, and rotating the upper body. To ensure that the noise generated by motion artifacts falls within the bandwidth of the band-pass filter and to test the effectiveness of the sample entropy method, subjects were asked to perform these actions at a frequency greater than 1.0 Hz and less than 1.5 Hz, which corresponds to the range of resting heart rates. Additionally, to simulate real-world motion artifacts, the order and number of these actions in the trial are not fixed. This study involves five subjects, with each subject participating in five trials. To validate the effectiveness of using sample entropy, we also process the signal without applying the sample entropy method, as a comparison. Specifically, among the top four highest-magnitude frequency components, the component with the highest magnitude within the resting heart rate range is selected as the heart rate component. As a control group, each subject's heart rate is monitored by PCERS while they are required to remain still. The heart rate measured by the Polar H10 served as the benchmark for these experiments. In the experimental group with motion artifact, the frequency difference between the component with the highest magnitude in the 0.6–3.0 Hz band and the heart rate frequency detected by the Polar H10 was examined and a mean difference of 19.83 bpm was found, indicating that fiber movements introduced artifacts that added noise to the HRV signal measurements.

Characterization and confirmation

The characteristics essential for precise cardiac activity monitoring were evaluated in this study. In addition to the previously mentioned robustness against motion artifacts, we also assessed PVSD's response to vibrations of varying intensities, its durability, and its resistance to ambient light through a series of experiments.

To assess PVSD's response to vibrations of varying intensities. A elastic ball was dropped from a series of heights (5 cm, 10 cm, 15 cm, 20 cm, 25 cm, and 30 cm) to impact it. The peak amplitude of the signal pulse resulting from the ball's impact is illustrated in Supplementary information of Fig. S10(a). The data indicate that the peak amplitude of the signal pulse increases in an approximately linear manner with the height from which the elastic ball is dropped, exhibiting a coefficient of determination of $R^2 = 0.92$.

Similar to the experiment validating SCG signal extraction under motion artifacts, the tests assessing PVSD's durability and resistance to ambient light were conducted with five subjects, using the heart rate measured by the Polar H10 as the benchmark. In the durability assessment phase, we evaluated the performance of PVSD immediately after manufacturing and again after 3 months of utilization. The results for the accuracy of heart rate monitoring and the SNR of the SCG signal are presented in Supplementary information of Fig. S13(a, b). It is observed that both the accuracy and SNR remain stable. The mean accuracy for heart rate monitoring was 99.64% immediately after manufacturing and 99.66% after 3 months of utilization, while the mean SNR values were 14.92 dB and 14.75 dB, respectively. These results demonstrate the high durability of PVSD's performance in obtaining clean and accurate SCG signals. In the evaluation of PVSD's robustness against ambient light, PVSD's performance in both bright and dark environments was assessed. The results of these experiments are illustrated in Supplementary inforamtion of Fig. S13(c, d). It is evident that whether ambient light is present or not, the accuracy of heart rate monitoring and the SNR of SCG signals remained stable. The mean accuracy for heart rate monitoring was 99.64% in bright conditions and 99.50% in dark conditions, while the mean SNR values were 14.92 dB and 14.15 dB, respectively. It is noteworthy that both the accuracy and SNR are higher in bright conditions with ambient light than in dark conditions. This leads to the conclusion that PVSD is largely unaffected by ambient light.

Feature extraction

In this study, we extracted three types of features as inputs for the machine learning model.

SCG network features

1) AC: the assortativity coefficient, defined as the Pearson correlation coefficient of degrees between pairs of connected nodes[57], reflects a node's tendency to connect with other nodes of similar degree within a network.

2) ASP: the average shortest path length is the mean number of steps along the shortest paths between all possible node pairs in a network.

3) BC: betweenness centrality measures a node's importance by summing the ratios of shortest paths that pass through it to the total number of shortest paths between all node pairs. In this study, we computed the average betweenness centrality across all nodes.

4) GCC: the global clustering coefficient, defined as the ratio of closed triplets to the total number of triplets in a network, giving an indication of the overall clustering tendency within the network.

Time-domain HRV

1) PNN20: the proportion of successive *NN* interval pairs that differ by more than 20 ms, divided by the total number of *NN* intervals, where an *NN* interval represents the time between two consecutive heartbeats.

2) RMSSD: the square root of the mean squared differences between adjacent *NN* intervals.

3) SDNN: the standard deviation of *NN* intervals.

4) SDSD: the standard deviation of the differences between successive *NN* intervals.

Traditional nonlinear features

1) Poincaré plot: features extracted from the Poincaré plot constructed from the SCG signal, including SD1, SD2, and SD2/SD1. Calculation methods are detailed in the Supplementary information of Supplementary section 1.

2) DFA: features extracted by detrended fluctuation analysis, including DFA1 and DFA2. The calculation details are provided in the Supplementary information of Supplementary section 2.

3) Sample entropy: same calculation method as aforementioned. Sampen1 and Sampen2 correspond to $l = 1$ and $l = 2$, respectively.

Pipeline for each fold of cross-validation

For each fold of cross-validation, the dataset is first split into training and test sets according to the specific cross-validation method. A data scaler is then fitted on the training set and applied to scale both the training and test sets independently. Following this, feature selection models are trained on the training set, and features are selected based solely on the training data. Finally, a classifier is trained on the selected features from the training set and evaluated on the test set to produce the emotion recognition results.

Permutation importance and feature selection

Permutation importance is computed by randomly shuffling individual features in the dataset and measuring the resulting change in emotion recognition accuracy relative to the original (non-shuffled) data. In each fold of cross-validation, the permutation importance for the valence and arousal dimensions is calculated separately on the training dataset. Based on these importance scores, eight features are selected from the original fifteen. The model is then trained using the selected features and evaluated on the corresponding features in the test dataset. The selection frequency of each feature across different cross-validation methods is presented in the Supplementary information of Fig. S2. Traditional HRV features (SDNN, PNN20) and SCG network features (GCC, AC, ASP, and BC) were found to have the highest selection frequencies.

Machine learning model

The machine learning model used in this study is an SVM.

To enhance its nonlinear classification capability, a radial basis function (RBF) kernel is employed. In addition to SVM with RBF kernel, the performance of other machine learning models, including linear SVM, XGBoost, and K-Nearest Neighbors (KNN), was also evaluated. The accuracy gap of these classifiers between subject-independent and subject-dependent emotion recognition remain a low level. These results are detailed in the Supplementary information of Figs. S5–S7.

Methods of statistical analysis

The analysis of differences in extracted features across different emotions consists of the following steps. The Kolmogorov-Smirnov (KS) test was employed to assess whether the feature distributions followed a normal distribution. In cases of normal distribution, repeated measures (RM) ANOVA tests were employed to assess whether there were significant differences in the extracted features across the four emotions: fear, joy, relaxation, and sadness. Pairwise Tukey tests were then conducted as post-hoc analyses to examine the differences in features between each pair of emotions. In cases of non-normal distribution, nonparametric analyses, including Friedman tests and Wilcoxon signed-rank tests, were employed to determine whether there were significant differences in the features across emotions and to assess pairwise differences between emotions, respectively. All these tests were performed on normalized features.

In the statistical analysis of subject variations, RM ANOVA tests were employed to assess whether there were significant differences in features across different subjects in the cases of normal distribution, while Friedman tests were used for non-normal distribution cases.

Conclusions

In this work, we proposed a cardiac activity-based emotion recognition system. In the signal extraction component, the use of a polymer optical fiber (POF) sensor demonstrated several advantages, including rapid response and recovery times (15.09 ms and 11.32 ms, respectively), as well as high robustness (maintaining consistent performance after three months of use). The sample entropy-based signal processing pipeline effectively captures the complexity of signal components and suppresses in-band noise caused by motion artifacts, achieving a heart rate monitoring accuracy of 98.32% under motion artifact conditions. In comparison, the method without sample entropy achieved only 91.55%. Furthermore, the system attained an accuracy of 99.64% under artifact-free conditions. These results demonstrating the effectiveness of incorporating sample entropy in the signal processing pipeline. In the emotion recognition component, topological features extracted from networks constructed using SCG signals exhibited significant differences across emotional states (all p-values < 0.05), while showing no significant variation across subjects (all p-values > 0.05). In contrast, some traditional time-domain HRV and nonlinear features displayed significant differences across subjects. This subject-invariant characteristic of the network-based features contributes to the high performance of our model in cross-subject emotion recognition, achieving accuracies of 81.25% and 77.98% under LOO and LTO cross-validation, respectively. Moreover, the accuracy gap between subject-dependent and subject-independent emotion recognition in our study was only 1.04% and 2.75% in two respective comparison settings—substantially lower than the 14.7% gap reported in a previous study[23].

For the complex network features, we provide a hypothesis regarding the potential association between the network-based features and autonomic neural regulation. The constructed complex network primarily encodes the similarity relationships among successive heartbeat intervals, thereby characterizing the global organization of inter-beat dynamics. We speculate that such similarity patterns may reflect the coordinated modulation of cardiac rhythm by the autonomic nervous system under different emotional states. However, this interpretation remains preliminary and requires further physiological validation. We should further clarify that the network-based features are not inherently more sensitive than traditional HRV features, but instead exhibit greater consistency across subjects, as supported by both the machine learning and statistical results. This may be because they capture pairwise relative relationships between heartbeat intervals, which are less influenced by individual baseline differences. Further studies are needed to substantiate this explanation.

For future work, we will explore the potential of this complex network feature engineering framework in other quasi-periodic biosignals, such as respiration, gait cycles, and blood pressure fluctuations, as well as its applications beyond emotion recognition. Speckle pattern technology can also be utilized to detect hemodynamic activity in the brain. We will attempt to simultaneously measure both cerebral hemodynamic and cardiac activity using this technology to explore the relationship between the brain and heart during emotional arousal. Furthermore, considering the system's robustness to motion artifacts and inter-subject variability, we plan to evaluate its emotion recognition performance in real-world, daily-life application scenarios. Given PCERS's ability to decode subject-invariant emotional information and further mitigate limitations in subject-independent emotion recognition, we believe it holds potential to contribute meaningfully to practical, real-world emotion recognition applications in the future.

References

1. Bijanzadeh M, Khambhati AN, Desai M et al. Decoding naturalistic affective behaviour from spectro-spatial features in multiday human iEEG. *Nat Hum Behav* **6**, 823-836 (2022).

2. Lincoln TM, Schulze L, Renneberg B. The role of emotion regulation in the characterization, development and treatment of psychopathology. *Nat Rev Psychol* **1**, 272-286 (2022).
3. Picard RW, Vyzas E, Healey J. Toward machine emotional intelligence: analysis of affective physiological state. *IEEE Trans Pattern Anal Mach Intell* **23**, 1175-1191 (2001).
4. Calvo RA, D'Mello S. Affect detection: an interdisciplinary review of models, methods, and their applications. *IEEE Trans Affect Comput* **1**, 18-37 (2010).
5. Shanechi MM. Brain-machine interfaces from motor to mood. *Nat Neurosci* **22**, 1554-1564 (2019).
6. Zepf S, Hernandez J, Schmitt A et al. Driver emotion recognition for intelligent vehicles: a survey. *ACM Comput Surv* **53**, 64 (2020).
7. Yu SZ, Androsov A, Yan HB et al. Bridging computer and education sciences: a systematic review of automated emotion recognition in online learning environments. *Comput Educ* **220**, 105111 (2024).
8. Yitzhak HL, Kelman YT, Moskovenko A et al. Emotion recognition using speckle pattern analysis and *k*-nearest neighbors classification. *J Opt* **23**, 015302 (2021).
9. Lee JP, Jang H, Jang Y et al. Encoding of multi-modal emotional information via personalized skin-integrated wireless facial interface. *Nat Commun* **15**, 530 (2024).
10. Cowen AS, Laukka P, Elfenbein HA et al. The primacy of categories in the recognition of 12 emotions in speech prosody across two cultures. *Nat Hum Behav* **3**, 369-382 (2019).
11. Bradley MM, Lang PJ. Measuring emotion: the self-assessment manikin and the semantic differential. *J Behav Ther Exp Psychiatry* **25**, 49-59 (1994).
12. Koelstra S, Muhl C, Soleymani M et al. DEAP: a database for emotion analysis; using physiological signals. *IEEE Trans Affect Comput* **3**, 18-31 (2012).
13. Ekman PE, Davidson RJ. *The Nature of Emotion: Fundamental Questions* (Oxford University Press, New York, 1994).
14. Candia-Rivera D, Catrambone V, Thayer JF et al. Cardiac sympathetic-vagal activity initiates a functional brain-body response to emotional arousal. *Proc Natl Acad Sci USA* **119**, e2119599119 (2022).
15. Hsueh B, Chen R, Jo Y et al. Cardiogenic control of affective behavioural state. *Nature* **615**, 292-299 (2023).
16. Bayoumy K, Gaber M, Elshafeey A et al. Smart wearable devices in cardiovascular care: where we are and how to move forward. *Nat Rev Cardiol* **18**, 581-599 (2021).
17. Agrafioti F, Hatzinakos D, Anderson AK. ECG pattern analysis for emotion detection. *IEEE Trans Affect Comput* **3**, 102-115 (2012).
18. Hsu YL, Wang JS, Chiang WC et al. Automatic ECG-based emotion recognition in music listening. *IEEE Trans Affect Comput* **11**, 85-99 (2020).
19. Nardelli M, Valenza G, Greco A et al. Recognizing emotions induced by affective sounds through heart rate variability. *IEEE Trans Affect Comput* **6**, 385-394 (2015).
20. Harper R, Southern J. A Bayesian deep learning framework for end-to-end prediction of emotion from heartbeat. *IEEE Trans Affect Comput* **13**, 985-991 (2022).
21. Hassan MM, Alam GR, Uddin Z et al. Human emotion recognition using deep belief network architecture. *Inf Fusion* **51**, 10-18 (2019).
22. Choi J, Hwang G, Lee JS et al. Weighted knowledge distillation of attention-LRCN for recognizing affective states from PPG signals. *Exp Syst Appl* **233**, 120883 (2023).
23. Li M, Li JZ, Chen YB et al. Stress severity detection in college students using emotional pulse signals and deep learning. *IEEE Trans Affect Comput* **16**, 1942-1954 (2025).
24. Zhao MM, Adib F, Katabi D. Emotion recognition using wireless signals. In *Proceedings of the 22nd Annual International Conference on Mobile Computing and Networking* 95–108 (ACM, 2016). https://doi.org/10.1145/2973750.2973762.
25. Gouveia C, Tomé A, Barros F et al. Study on the usage feasibility of continuous-wave radar for emotion recognition. *Biomed Signal Process Control* **58**, 101835 (2020).
26. Imran N, Zhang J, Ali J et al. mm-HrtEMO: non-invasive emotion recognition via heart rate using mm-wave sensing in diverse scenarios. *IEEE J Biomed Health Inf*, 1-12 (2024).
27. Can YS, Mahesh B, André E. Approaches, applications, and challenges in physiological emotion recognition—a tutorial overview. *Proc IEEE* **111**, 1287-1313 (2023).
28. Pan J, Wang Q, Gao SK et al. Knot-inspired optical sensors for slip detection and friction measurement in dexterous robotic manipulation. *Opto-Electron Adv* **6**, 230076 (2023).
29. Li Z, Chen JX, Li LZ et al. Exceptional-point-enhanced sensing in an all-fiber bending sensor. *Opto-Electron Adv* **6**, 230019 (2023).
30. Jha R, Mishra P, Kumar S. Advancements in optical fiber-based wearable sensors for smart health monitoring. *Biosens Bioelectron* **254**, 116232 (2024).
31. Li LY, Liu YF, Song CY et al. Wearable alignment-free microfiber-based sensor chip for precise vital signs monitoring and cardiovascular assessment. *Adv Fiber Mater* **4**, 475-486 (2022).
32. Zhao T, Fu XL, Zhou YH et al. Noncontact monitoring of heart rate variability using a fiber optic sensor. *IEEE Internet Things J* **10**, 14988-14994 (2023).
33. Wang Z, Chen ZY, Ma L et al. Optical microfiber intelligent sensor: wearable cardiorespiratory and behavior monitoring with a flexible wave-shaped polymer optical microfiber. *ACS Appl Mater Interfaces* **16**, 8333-8345 (2024).
34. Wang ZX, Wang Z, Li D et al. High-quality semiconductor fibres via mechanical design. *Nature* **626**, 72-78 (2024).
35. Kuang RF, Wang Z, Ma L et al. Smart photonic wristband for pulse wave monitoring. *Opto-Electron Sci* **3**, 240009 (2024).
36. Li WB, Long YK, Yan YY et al. Wearable photonic smart wristband for cardiorespiratory function assessment and biometric identification. *Opto-Electron Adv* **8**, 240254 (2025).
37. Yin JY, Wang SL, Tat T et al. Motion artefact management for soft bioelectronics. *Nat Rev Bioeng* **2**, 541-558 (2024).
38. Li YX, Zhang YJ, Xiao Q et al. Quasi-periodic Gaussian process modeling of pseudo-periodic signals. *IEEE Trans Signal Process* **71**, 3548-3561 (2023).
39. Sarkar P, Etemad A. Self-supervised ECG representation learning for emotion recognition. *IEEE Trans Affect Comput* **13**, 1541-1554 (2022).
40. Shen XK, Liu XG, Hu X et al. Contrastive learning of subject-invariant EEG representations for cross-subject emotion recognition. *IEEE Trans Affect Comput* **14**, 2496-2511 (2023).
41. Gehr S, Russmann C. Shaping the future of cardiovascular medicine in the new era of wearable devices. *Nat Rev Cardiol* **19**, 501-502 (2022).
42. Zhong PX, Wang D, Miao CY. EEG-based emotion recognition using regularized graph neural networks. *IEEE Trans Affect Comput* **13**, 1290-1301 (2022).
43. Si XP, He H, Yu JY et al. Cross-subject emotion recognition brain-

computer interface based on fNIRS and DBJNet. *Cyborg Bionic Syst* **4**, 0045 (2023).

44. Morioka H, Kanemura A, Hirayama JI et al. Learning a common dictionary for subject-transfer decoding with resting calibration. *NeuroImage* **111**, 167-178 (2015).
45. He WW, Ye YL, Li YX et al. Online cross-subject emotion recognition from ecg via unsupervised domain adaptation. In *2021 43rd Annual International Conference of the IEEE Engineering in Medicine & Biology Society* 1001-1005 (IEEE, 2021). http://doi.org/10.1109/EMBC46164.2021.9630433.
46. Malik M, Bigger JT, Camm AJ et al. Heart rate variability: Standards of measurement, physiological interpretation, and clinical use. *European Heart Journal* **17**, 3, 354–381 (1996).
47. Sanderson K. Electronic skin: from flexibility to a sense of touch. *Nature* **591**, 685-687 (2021).
48. Bennett A, Beiderman Y, Agdarov S et al. Monitoring of vital biosigns by analysis of speckle patterns in a fabric-integrated multimode optical fiber sensor. *Opt Express* **28**, 20830-20844 (2020).
49. Romano C, Formica D, Schena E et al. Investigation of body locations for cardiac and respiratory monitoring with skin-interfaced inertial measurement unit sensors. *IEEE Sens J* **23**, 7806-7815 (2023).
50. Li LY, Sheng SF, Liu YF et al. Automatic and continuous blood pressure monitoring via an optical-fiber-sensor-assisted smartwatch. *PhotoniX* **4**, 21 (2023).
51. Clarke JM, Shelton JR, Venning GR et al. The rhythm of the normal human heart. *Lancet* **308**, 508-512 (1976).
52. Ram MR, Madhav KV, Krishna EH et al. A novel approach for motion artifact reduction in PPG signals based on AS-LMS adaptive filter. *IEEE Trans Instrum Meas* **61**, 1445-1457 (2012).
53. Kumar SP, Sriraam N, Benakop P et al. Entropies based detection of epileptic seizures with artificial neural network classifiers. *Exp Syst Appl* **37**, 3284-3291 (2010).
54. Zhang J, Sun JF, Luo XD et al. Characterizing pseudoperiodic time series through the complex network approach. *Phys D* **237**, 2856-2865 (2008).
55. Zhang J, Small M. Complex network from pseudoperiodic time series: topology versus dynamics. *Phys Rev Lett* **96**, 238701 (2006).
56. Kiran RM, Chakraborty S. PDMS microfluidics: a mini review. *J Appl Polym Sci* **137**, 48958 (2020).
57. Newman MEJ. Assortative mixing in networks. *Phys Rev Lett* **89**, 208701 (2002).

Acknowledgements

This research funded by the National Key R&D Program of China (2022YFE0140400), the National Natural Science Foundation of China (62405027, 62111530238, 62003046), supporting project of major scientific research projects of Beijing Normal University at Zhuhai (ZHPT2023007), and the work of R.M. was supported by the Tang Scholar of Beijing Normal University.

Author contributions

Y.K.L. and R.M. proposed the idea and carried out most of the experimental work. K.X. and Z.W. contributed in the preparation of device. L.F.L., X.L.L., and Z.H.L. provided support with the machine learning algorithm. Y.F.S. and Z.Z. assisted with the optical technologies utilized in this work. All authors contributed to the discussion and writing of the manuscript.

Competing interests

The authors declare no competing financial interests.

Ethical statement

The protocol of this study was approved by the Department of Psychology, Beijing Normal University (No. 20250224003).

Supplementary information

Supplementary information for this paper is available at https://doi.org/10.29026/oet.2025.250010

Published by Editorial Office of *Opto-Electronic Technology*, Institute of Optics and Electronics, Chinese Academy of Sciences.